# Transmissivity and Reflectivity of a TE-polarized Wave Incident on a Microcavity Containing Strongly Coupled Excitons with In-plane Uniaxially Oriented Transition Dipole Moments

*F. Le Roux* R. A. Taylor D. D. C. Bradley*

F. Le Roux

Department of Physics, University of Oxford, Parks Road, Oxford, OX1 3PU, U.K.

Email Address: florian.leroux@physics.ox.ac.uk

R. A. Taylor

Department of Physics, University of Oxford, Parks Road, Oxford, OX1 3PU, U.K.

D. D. C. Bradley

Physical Science and Engineering Division, King Abdullah University of Science and Technology, Thuwal, 23955-6900, Saudi Arabia

Department of Physics, University of Oxford, Parks Road, Oxford, OX1 3PU, U.K.

Keywords: *exciton-polaritons, conjugated polymer microcavities, organic semiconductors, liquid crystalline conjugated polymer*

This work examines the reflectivity and transmissivity of a TE-polarized wave incident on a

microcavity containing strongly coupled excitons with in-plane uniaxially oriented transition dipole moments and presents a different interpretation to a previous report. The propagation of the electric field inside the cavity is discussed and a distinction is made between two different physical cases: the first, previously observed, and the second, which enables the interpretation of measurements performed on a microcavity containing an oriented layer of liquid-crystalline poly(9,9-dioctylfluorene). In all cases, the reflected and transmitted electric fields derive from photons leaking parallel and perpendicular to the transition dipole moment orientation.



# 1 Introduction

Exciton-polaritons in solid state microcavities are an active field of research thanks to their potential for both fundamental (Bose Einstein condensation [1, 2, 3], light superfluidity [4, 5]) and practical applications (optical transistors [6], exciton-polariton lasers [7, 8], light-emitting diodes [9]). Since their first observation [10] in a planar microcavity, in which an excitonic medium is sandwiched between two mirrors, a wide variety of materials including III-V [10] and II-VI [11] inorganic semiconductors, semiconducting conjugated polymers [12], small molecules [13], perovskite [14] and 2D-materials [15] have been used for their fabrication.

Strongly coupled microcavities contain layers of material whose optical refractive indices, shaped by the physical properties of the excitons, can exhibit different forms of anisotropy. The exciton transition dipole moment $\mu$ can for example lie parallel to the mirrors [16] (in-plane/out-of-plane anisotropy) where it can further adopt a preferential orientation (in-plane uniaxial anisotropy), for instance along crystalline axes. [17] Recent experimental demonstrations of strong coupling (SC) using oriented J-aggregates, [18] nanotubes (made of carbon [19] or tungsten disulfide [20]), liquid crystals [21] and liquid crystal conjugated polymers (LCCP)s [22] have been reported and study the influence of orienting $\mu$ on the resulting polaritons.

Fitting the energy dispersions of the minima (maxima) of the reflected (transmitted) intensity

spectra obtained by varying the polar angle $\theta$ (shown in Figure 0) is usually sufficient to characterize the strength of the interaction taking place inside a microcavity, as increasing $\theta$ is equivalent to increasing the cavity mode energy, which close to the excitonic resonance splits into two extrema, the lower and upper polaritons (LP, UP) separated by the Rabi-splitting energy $\hbar\Omega_R$. For microcavities containing excitons whose transition dipole moments are oriented in-plane along a given direction, the interpretation of the transmissivity and reflectivity spectra is less straightforward as the electric field in the polaritonic modes becomes fully concentrated along the transition dipole moment, a result previously demonstrated by Litinskaya *et al.* [23] and Balagurov *et al*. [24]

Here, we examine the specific case of a TE-polarized wave incident on a microcavity containing strongly coupled excitons with $\boldsymbol{\mu}$ oriented along $\mathbf{e}_y$ (see Figure 0). We focus on the effect of rotating the electric field $\mathrm{E}$ with respect to the azimuthal angle $\phi$ (represented in Figure 1) and show that in the presence of cavity damping broad enough compared with $\hbar\Omega_{0y}$ (the Rabi-splitting energy induced by the excitons in the $\mathbf{e}_y$ direction) the transmissivity and reflectivity exhibit two extrema which get closer in energy as $\phi$ is increased.

Whilst this result resembles the one obtained when increasing $\theta$ in strongly coupled microcavities where $\boldsymbol{\mu}$ has no preferential in-plane orientation, we show that the extrema are in fact the superposition of separate intensities originating from the propagation of two waves dephased by experiencing either the permittivity brought about by the excitons along $\mathbf{e}_y$ (yielding the LP and UP extrema) or the background permittivity along $\mathbf{e}_x$ (yielding a photonic mode extremum). We underline that this measurement has previously led to a different interpretation. [19]

When $\hbar\Omega_{0y}$ is much larger than the cavity damping, we recover signals in which the three extrema become clearly resolved and do not experience any spectral shift upon increase of $\phi$. We support our results by fabricating and measuring the TE-reflectivity from a metallic microcavity containing an oriented layer of liquid-crystalline poly(9,9-dioctylfluorene) (PFO).

## 2 TE-polarized Wave Propagation

We first examine the propagation of an incident TE-polarized wave inside a microcavity containing excitons with $\mu$ oriented along $\mathbf{e}_y$. The geometry is shown in Figure 1.

In the linear approximation, the dielectric permittivity tensor of the cavity layer takes the form:

$$\epsilon(\omega) = \epsilon_0 \begin{pmatrix} \epsilon_x & 0 & 0 \\ 0 & \epsilon_y & 0 \\ 0 & 0 & \epsilon_z \end{pmatrix} \quad (1)$$

where $\epsilon_0$ is the permittivity in vacuum. In the outside medium, a TE-polarized plane wave incident on the microcavity can be written:

$$\mathbf{E}_i(\mathbf{r}, t) = \mathbf{E}_{0_i} e^{-j[k_x x + k_y y + k_z z - \omega t]}, \quad (2)$$

where: $\mathbf{E}_{0_i} = E_{0_i x} e_x + E_{0_i y} e_y$. The propagation of TE-polarized waves in birefringent media is well documented [25, 26, 27]: if $\mathbf{E}_{0_i}$ is parallel to either $\mathbf{e}_x$ or $\mathbf{e}_y$ then the wave propagates experiencing the corresponding axis permittivity (see Figure 1 (b)), otherwise the $x$ and $y$ components propagate separately and are dephased according to the in-plane anisotropy of the medium.

We now focus on angle-resolved transmissivity and reflectivity spectra which commonly allow characterization of the SC regime. We take below the example of reflectivity but note that the reasoning and therefore results, are qualitatively similar for transmissivity. We use a Lorentzian model to represent the electric susceptibility of the excitons inside the cavity layer:

$$\chi(\omega) = \frac{4 g_0^2}{\omega_{ex}^2 - \omega^2 - j\gamma_{ex}\omega}, \quad (3)$$

where $g_0$ is the amplitude of the resonance, $\omega_{ex}$ is the transition pulse frequency of the exciton

and $\gamma_{ex}$ is the natural homogeneous broadening. The dielectric permittivity then reads:

$$\epsilon(\omega) = \epsilon_0 \begin{pmatrix} \epsilon_m & 0 & 0 \\ 0 & \epsilon_m(1+\chi(\omega)) & 0 \\ 0 & 0 & \epsilon_m \end{pmatrix}, \quad (4)$$

where $\epsilon_m$ is the background permittivity of the dielectric layer. We decompose the incoming wave along $\mathbf{e}_x$ and $\mathbf{e}_y$:

$$\mathbf{E}_{0_i} = |\mathbf{E}_{0_i}| \begin{pmatrix} -\sin\phi \\ \cos\phi \\ 0 \end{pmatrix}. \quad (5)$$

Similarly to what was noted by Balagurov *et al.* [24], the $\mathbf{e}_x$ component experiences the permittivity $\epsilon_x = \epsilon_0 \epsilon_m$ and the resulting wave is weakly coupled to the structure while the $\mathbf{e}_y$ component experiences the permittivity $\epsilon_y$ and the physics falls back to that of SC inside an hypothetical medium where $\epsilon_x = \epsilon_y = \epsilon_{ord}$, where $\epsilon_{ord}$ is the ordinary (in-plane) component of the permittivity, yielding the LP and UP (see Supporting Information Sections 1 and 2 for more details). The overall reflected electric field can then be written under the form:

$$\mathbf{E}_r = |\mathbf{E}_{0_i}| \begin{pmatrix} -r_x(\theta,\omega)\sin\phi \\ r_y(\theta,\omega)\cos\phi \\ 0 \end{pmatrix}, \quad (6)$$

where $r_x(\theta,\omega)$ and $r_y(\theta,\omega)$ can be fully determined using transfer matrix calculations (TMC)s. Since $r_x(\theta,\omega)$ and $r_y(\theta,\omega)$ are calculated using $\epsilon_x$ and $\epsilon_y$, they do not yield in-phase reflected waves except in very specific cases where the dimensions of the cavity allow matching of the phase-changes experienced in the two directions. Following averaging, the total reflected intensity becomes the sum of the weighted contributions along $\mathbf{e}_x$ and $\mathbf{e}_y$:

$$\mathbf{R}_r(\phi,\theta,\omega) = |r_x(\theta,\omega)|^2 \sin^2\phi + |r_y(\theta,\omega)|^2 \cos^2\phi, \quad (7)$$

which, as we will see in the next section, can lead to the existence of one to three minima (maxima

for transmissivity) that require careful interpretation.

## 3 Simulations

We can identify two cases using Equation 7 and the coupling considerations made in the previous section: (i) The photonic mode broadening along $\mathbf{e}_x$ is comparable to $\hbar\Omega_{0y}$ and the LP and UP extrema in reflectivity/transmissivity observed along $\mathbf{e}_y$ mix with the photonic mode extremum along $\mathbf{e}_x$ to form two peaks for $\phi \in ]0^\circ, 90^\circ[$ that converge towards the photonic mode energy as $\phi$ is increased; (ii) $\hbar\Omega_{0y}$ is intense enough so that the LP and UP along $\mathbf{e}_y$ are distant enough spectrally to not mix with the central photonic mode extremum along $\mathbf{e}_x$ resulting in three peaks for $\phi \in ]0^\circ, 90^\circ[$.

Figure 2 (b) shows the simulated transmissivity at normal incidence ($\theta = 0^\circ$) for an aluminium microcavity (Al thickness 100 nm at the bottom, 30 nm at the top) containing a 94.5 nm thick layer of material M1 whose susceptibility parameters are: $\epsilon_m = 2.56$, $\hbar\omega_{ex} = 3.25\text{eV}$, $g_0 = 4 \times 10^{12}\text{rads}^{-1}$ and $\gamma_{ex} = 10^{12}\text{rads}^{-1}$ (corresponding to a full width at half maximum (FWHM): $\hbar\gamma_{ex} \sim 0.7\text{meV}$). The cavity mode at normal incidence is slightly detuned $\hbar\Delta = \hbar(\omega_{ex} - \omega_{cav}) = 9.5\text{meV}$ and its broadening is $\hbar\kappa = 110\text{meV}$. The linewidths of the polaritons in the $e_y$ direction are measured : $\text{FWHM}_{UP/LP} \sim 55\text{meV}$ which is correctly predicted by: $\text{FWHM}_{UP/LP} = \hbar\frac{\kappa + \gamma_{ex}}{2}$ [28]. Following fitting (see Supporting Information Section 3), we derive: $\hbar\Omega_{0y} = 58\text{meV}$ which is resolved as $\hbar\Omega_{0y} > \hbar\frac{\kappa + \gamma_{ex}}{2}$.

For $\phi \in ]0^\circ, 90^\circ[$, since $\hbar\Omega_{0y} + \text{FWHM}_{UP/LP} < \hbar\kappa$, the transmissivity is composed of two peaks with each peak being the sum of one polariton and the overlapping photonic mode

transmissivities mixed together thanks to the large value of $\hbar\kappa$ : this situation corresponds to the first physical case previously identified. As $\phi$ is increased, the relative transmissivity of the photonic mode along $\mathbf{e}_x$ increases while the transmissivities of the polaritons along $\mathbf{e}_y$ decrease bringing the peaks closer until they give way to the cavity mode at $3.2405\text{eV}$ for $\phi = 90^\circ$. This phenomenon is fully explained by Equation 7 as the two squared trigonometric functions vary in opposite fashion upon increase of $\phi$ and the respective contributions from the two directions can be observed as dashed lines in Figure 2 (b).

The extrema dispersions are represented in Figure 2 (c), for $\phi \in ]0^\circ, 90^\circ[$, we further note that each transmissivity maximum derive from orthogonal contributions along $\mathbf{e}_x$ and $\mathbf{e}_y$ and as such does not characterize an eigenmode of the structure. This first transmissivity analysis offers an explanation to a previous experimental observation [19].

Figure 3 (b) shows the simulated transmissivity at normal incidence ($\theta = 0^\circ$) for an aluminium microcavity (Al thickness 100 nm at the bottom, 30 nm at the top) containing a 94.5 nm thick layer of material M2 whose susceptibility parameters are: $\epsilon_m = 2.56$, $\hbar\omega_{ex} = 3.25$ eV, $g_0 = 10^{14}\text{rads}^{-1}$ and $\gamma_{ex} = 4\times10^{13}\text{rads}^{-1}$ (corresponding to a $\text{FWHM} = \hbar\gamma_{ex} \sim 26\text{meV}$). For this structure, $\hbar\Omega_{0y}$ is fitted: $\hbar\Omega_{0y} = 1.38\text{eV}$. This splitting represents $\sim 42\%$ of the exciton energy $\hbar\omega_{ex} = 3.25\text{eV}$ bringing the system into ultrastrong coupling (USC) along $\mathbf{e}_y$. $\hbar\kappa$ is this time more than one order of magnitude smaller than $\hbar\Omega_{0y}$ and $\hbar\Omega_{0y} + \text{FWHM}_{\text{UP/LP}} \gg \hbar\kappa$, the transmissivity now resolves three peaks for $\phi \in ]0^\circ, 90^\circ[$ which are the two polaritons and the photonic mode transmissivities weighted by $\phi$ (Equation 7). As $\phi$ is increased, the relative transmissivity of the photonic mode along $\mathbf{e}_x$ increases while the transmissivities of the polaritons along $\mathbf{e}_y$ decrease changing the relative heights of the peaks without spectrally shifting them corresponding to the

second physical case previously identified. The extrema positions are represented in Figure 3 (c).

We note that the TE-transmissivity values obtained in Figure 2 (b) and Figure 3 (b) are too low to be actually measured. Figure 4 (a) and (b) represent simulated TE-reflectivities for similar structures differing in a 99.5 nm thick cavity layer and the measurement being performed at $\theta = 30^{\circ}$ to keep the detuning at $\Delta = 10\,meV$. The origin of the minima observed are analog to the maxima in transmissivity and the interpretation is identical to the one previously made. We then proceed in the following section to fabricate and measure a microcavity with similar characteristics to the one showed in Figure 3 (c), corresponding to the second physical case previously identified.

## 4 Experimental Comparison with a Microcavity Containing an Oriented Layer of PFO

We fabricated a microcavity containing a layer of PFO whose chains were oriented along $\mathbf{e}_y$ thanks to the use of a photoalignment-layer-induced homogeneous nematic orientation technique [29, 22], the structure and orientation are shown in Figure 5 (a) and (b), the exact fabrication process is detailed elsewhere [22]. The refractive index of the oriented PFO is reproduced from Ref 22 and shown in Supporting Information. The coupling strength for $E$ parallel to $\mathbf{e}_y$ is almost identical to the one derived in Ref 22 (see Supporting Information Section 4 for derivation) and TMCs confirm the dimensions of the structure for both simulations and experiments with zero detuning between cavity mode and exciton (centered at $3.25\,eV$) reached for $\theta = 46^{\circ}$.

A few differences exist between this system and the simulations presented in the previous section: (i) The permittivity of the embedded layer is not strictly identical to the one used in Equation 4 as there exists remainding optical activity along $\mathbf{e}_x$, however much less intense than along $\mathbf{e}_y$; (ii) The exciton spectral distribution is inhomogeneously broadened (as a result of deviations from the

mean fluorene-fluorene single bond torsion angle ($\sim 135^{\circ}$) [30]) but this broadening does not alter the value of $\hbar\Omega_{0y}$ [31, 32, 22].

Figure 5 (c) shows the simulated TE-transmissivity for $\theta = 46^{\circ}$ for increasing values of $\phi = 0^{\circ}, 18^{\circ}, 36^{\circ}, 54^{\circ}, 72^{\circ}, 90^{\circ}$. At $\phi = 0^{\circ}$, $\mathbf{E}$ is parallel to $\mathbf{e}_y$ and we observe two intense maxima (1 and 3) that correspond to the LP and UP. Interestingly, we also observe the formation of another peak (2) close to the LP at $\sim 2.95\text{eV}$ which corresponds to a further LP brought about by SC of the second lowest lying cavity mode with the excitons (this coupling is made possible thanks to the intense absorption in the $\mathbf{e}_y$ direction), this shoulder peak is shown in more detail in the inset of Figure 5 (c).

For $\phi \in ]0^{\circ}, 90^{\circ}[$, we observe the formation of four maxima. The two most outer ones in energy correspond to the LP and UP transmissivities identified as peaks 1 and 3 created by SC of the lowest lying cavity mode to the excitons. Given the large value of $\hbar\Omega_{0y} = 1.47\text{eV}$ compared with the cavity mode broadening $\hbar\kappa = 220\text{meV}$ those maxima are similar in nature to those in Figure 3 (b) and consequently do not shift in energy as $\phi$ is increased.

The two remaining maxima are better understood by examining $\phi = 90^{\circ}$. For this angle, $\mathrm{E}$ is perpendicular to $\mathbf{e}_y$ and the remaining optical activity along $\mathbf{e}_x$ causes the photonic mode to split around the exciton at 3.25 eV (peak 4 at 3.0 eV and peak 5 at 3.67 eV). Maxima 4 and 5 are not clearly resolved since the oscillator strength along $\mathbf{e}_x$ is not intense enough following orientations of the PFO chains, as it was demonstrated in Ref 22 that the broad and unstructured emission from this structure confirmed weak coupling along $\mathbf{e}_x$.

For $\phi \in ]0^{\circ}, 90^{\circ}[$, the second lowest maximum in energy is the superposition of peaks 2 and 4, 0.05 eV apart in energy, whose respective broadenings allow for their mixing, with the overall maximum seemingly shifting to lower energies as $\phi$ is increased. Finally, the third lowest maximum in energy corresponds to peak 5 and does not shift with increasing $\phi$.

Figure 5 (d) shows the experimental measurement of the TE-reflectivity at $\theta = 46^\circ$. All the minima are similar to the maxima identified using the simulated TE-transmissivity in Figure 5 (c) and their spectral positions is confirmed by simulating the TE-reflectivity in Figure 5 (e).

# 5 Conclusion

We have carefully examined the effects of rotating the electric field with respect to $\phi$ for an incident TE-polarized wave on the measured reflectivity and transmissivity of a microcavity containing strongly coupled excitons with in-plane uniaxially oriented transition dipole moments. We have demonstrated that when the cavity damping $\hbar\kappa$ is broad enough compared to $\hbar\Omega_{0y}$, TE-transmissivity and reflectivity present two extrema for $\phi \in ]0^\circ, 90^\circ[$ which get closer in energy as $\phi$ is increased. While this resembles the result obtained upon increase of the polar angle $\theta$ when the transition dipole moment has no preferential in-plane orientation, these extrema are the superposition of separate intensities originating from the propagation of two waves experiencing either SC along $\mathbf{e}_y$ or weak coupling along $\mathbf{e}_x$ but mixed thanks to the losses $\hbar\kappa$. This experimental observation was reported for oriented carbon nanotubes [19] and this work offers a physical interpretation. In the case where $\hbar\Omega_{0y}$ is much larger than the cavity damping, we showed that the measured reflectivity and transmissivity present three extrema for $\phi \in ]0^\circ, 90^\circ[$ which are the separate contributions from the different directions, as such they do not experience any spectral shifting with increasing $\phi$. We supported our analytical model by fabricating and measuring the TE-reflectivity from a metallic microcavity containing an oriented layer of liquid-crystalline PFO and interpreted the different extrema observed by considering separately the contributions from the $\mathbf{e}_x$ and $\mathbf{e}_y$ directions.

**Supporting Information**

Supporting Information is available from the Wiley Online Library or from the author.

**Acknowledgements**

The authors acknowledge funding from the University of Oxford, from the UK Engineering and Physical Sciences Research Council and the Jiangsu Industrial Technology Research Institute. F.L.R. further thanks Wolfson College and Dr Simon Harrison for the award of a Wolfson Harrison UK Research Council Physics Scholarship.



# References

[1] J. Kasprzak, M. Richard, S. Kundermann, A. Baas, P. Jeambrun, J. M. J. Keeling, F. M. Marchetti, M. H. Szymańska, R. André, J. L. Staehli, V. Savona, P. B. Littlewood, B. Deveaud, L. S. Dang, *Nature* **2006**, *443*, 7110 409.

[2] J. D. Plumhof, T. Stöferle, L. Mai, U. Scherf, R. F. Mahrt, *Nature Materials* **2014**, *13*, 3 247.

[3] K. S. Daskalakis, S. A. Maier, R. Murray, S. Kéna-Cohen, *Nature Materials* **2014**, *13*, 3 271.

[4] A. Amo, J. Lefrère, S. Pigeon, C. Adrados, C. Ciuti, I. Carusotto, R. Houdré, E. Giacobino, A. Bramati, *Nature Physics* **2009**, *5*, 11 805.

[5] G. Lerario, D. Ballarini, A. Fieramosca, A. Cannavale, A. Genco, F. Mangione, S. Gambino, L. Dominici, M. De Giorgi, G. Gigli, D. Sanvitto, *Light: Science & Applications* **2017**, *6*, 2

e16212.

[6] A. V. Zasedatelev, A. V. Baranikov, D. Urbonas, F. Scafirimuto, U. Scherf, T. Stöferle, R. F. Mahrt, P. G. Lagoudakis, *Nature Photonics* **2019**, *13*, 6 378.

[7] P. Bhattacharya, B. Xiao, A. Das, S. Bhowmick, J. Heo, *Physical Review Letters* **2013**, *110*, 20 206403.

[8] S. Kéna-Cohen, S. R. Forrest, *Nature Photonics* **2010**, *4*, 6 371.

[9] M. Mazzeo, A. Genco, S. Gambino, D. Ballarini, F. Mangione, O. Di Stefano, S. Patanè, S. Savasta, D. Sanvitto, G. Gigli, *Applied Physics Letters* **2014**, *104*, 23 233303.

[10] C. Weisbuch, M. Nishioka, A. Ishikawa, Y. Arakawa, *Physical Review Letters* **1992**, *69*, 23 3314.

[11] P. Kelkar, V. Kozlov, H. Jeon, A. V. Nurmikko, C.-C. Chu, D. C. Grillo, J. Han, C. G. Hua, R. L. Gunshor, *Physical Review B* **1995**, *52*, 8 R5491.

[12] D. G. Lidzey, D. D. C. Bradley, M. S. Skolnick, T. Virgili, S. Walker, D. M. Whittaker, *Nature* **1998**, *395*, 6697 53.

[13] R. J. Holmes, S. R. Forrest, *Physical Review Letters* **2004**, *93*, 18 186404.

[14] T. Fujita, Y. Sato, T. Kuitani, T. Ishihara, *Physical Review B* **1998**, *57*, 19 12428.

[15] X. Liu, T. Galfsky, Z. Sun, F. Xia, E.-c. Lin, Y.-H. Lee, S. Kéna-Cohen, V. M. Menon,

*Nature Photonics* **2015**, *9*, 1 30.

[16] S. Kéna-Cohen, S. A. Maier, D. D. C. Bradley, *Advanced Optical Materials* **2013**, *1*, 11 827.

[17] S. Kéna-Cohen, M. Davanço, S. R. Forrest, *Physical Review Letters* **2008**, *101*, 11 116401.

[18] D. N. Krizhanovskii, R. Butté, L. G. Connolly, A. I. Tartakovskii, D. G. Lidzey, M. S. Skolnick, S. Walker, *Journal of Applied Physics* **2003**, *93*, 9 5003.

[19] W. Gao, X. Li, M. Bamba, J. Kono, *Nature Photonics* **2018**, *12*, 6 362.

[20] L. Yadgarov, B. Višić, T. Abir, R. Tenne, A. Y. Polyakov, R. Levi, T. V. Dolgova, V. V. Zubyuk, A. A. Fedyanin, E. A. Goodilin, T. Ellenbogen, R. Tenne, D. Oron, *Physical Chemistry Chemical Physics* **2018**, *20*, 32 20812.

[21] M. Hertzog, P. Rudquist, J. A. Hutchison, J. George, T. W. Ebbesen, K. Börjesson, *Chemistry - A European Journal* **2017**, *23*, 72 18166.

[22] F. Le Roux, R. A. Taylor, D. D. C. Bradley, *ACS Photonics* **2020**.

[23] M. Litinskaya, P. Reineker, V. M. Agranovich, *physica status solidi (a)* **2004**, *201*, 4 646.

[24] D. B. Balagurov, G. C. La Rocca, *physica status solidi (c)* **2004**, *1*, 3 518.

[25] T. Scharf, *Polarized Light in Liquid Crystals and Polymers*, John Wiley & Sons, Inc., Hoboken, NJ, USA, **2006**.

[26] S. J. Orfanidis, *http://eceweb1.rutgers.edu/orfanidi/ewa/* .

[27] P. Yeh, *Journal of the Optical Society of America* **1979**, *69*, 5 742.

[28] Y. Zhu, D. J. Gauthier, S. E. Morin, Q. Wu, H. J. Carmichael, T. W. Mossberg, *Physical Review Letters* **1990**, *64*, 21 2499.

[29] H. Zhang, L. Ma, Q. Zhang, Y. Shi, Y. Fang, R. Xia, W. Hu, D. D. C. Bradley, *Advanced Optical Materials* **2020**, 1901958.

[30] W. Chunwaschirasiri, B. Tanto, D. L. Huber, M. J. Winokur, *Physical Review Letters* **2005**, *94*, 10 107402.

[31] R. Houdré, R. P. Stanley, M. Ilegems, *Physical Review A* **1996**, *53*, 4 2711.

[32] V. Savona, C. Weisbuch, *Physical Review B* **1996**, *54*, 15 10835.

**Table of Contents: This work examines the reflectivity and transmissivity of a TE-polarized wave incident on a microcavity containing strongly coupled excitons with in-plane uniaxially oriented transition dipole moments and demonstrate that the reflected and transmitted electric fields derive from photons leaking parallel and perpendicular to the transition dipole moment orientation.**

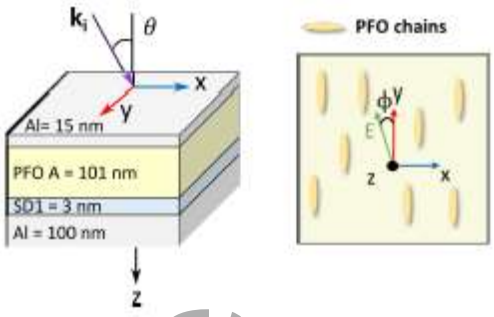


Representation of a TE-polarized wave incident on a microcavity containing an oriented layer of PFO, details on the geometry can be found in the main text.

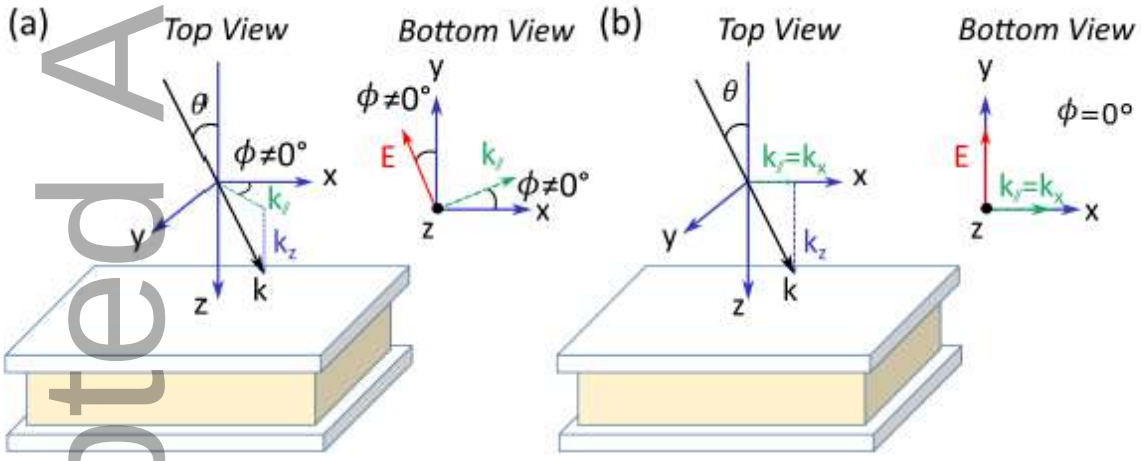


Figure 1: Geometry and angles used in this work, $\theta$ is the polar angle formed between **k** and $\mathbf{e}_z$, for a TE-polarized wave $\phi$ is the azimuthal angle formed between $\mathrm{E}$ and $\mathbf{e}_y$, and $\mathbf{k}_{//}$ is the in-plane component of the wavevector **k**. In (a) $\phi \neq 0^\circ$, in (b) $\phi = 0^\circ$: $\mathrm{E}$ is parallel to the transition dipole moment $\mu$ of the excitons and the wave propagates experiencing $\epsilon_y$, a similar situation arises for $\phi = 90^\circ$, where $\mathrm{E}$ becomes parallel to $\mathbf{e}_x$ and the wave experiences $\epsilon_x$.

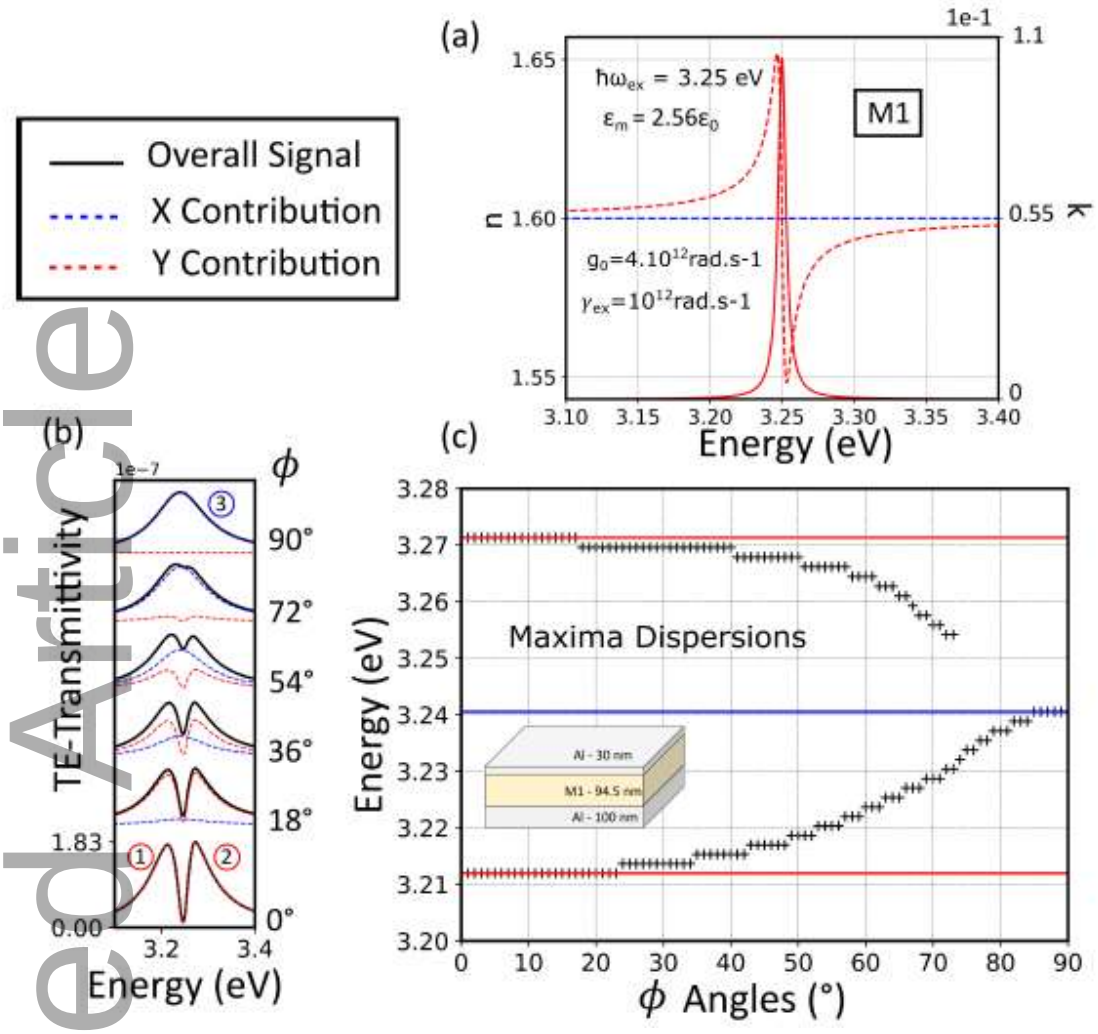


Figure 2: (a) In red and blue respectively ($n_y$, $k_y$) and ($n_x$, $k_x$) optical components for a simulated material M1 with susceptibility $\chi(\omega)$ using the physical parameters in the inset. Dashed lines give the real component of the complex refractive index $\tilde{n} = n + jk$, solid lines the imaginary component. (b) Simulated TE-transmissivity at $\theta = 0^\circ$ for $\phi = 0^\circ, 18^\circ, 36^\circ, 54^\circ, 72^\circ, 90^\circ$ of the microcavity displayed in the inset of (c), the black curves represents the total transmissivity which is a superposition of the transmissivities originating from the $\mathbf{e}_y$ direction (in dashed red) and $\mathbf{e}_x$ direction (in dashed blue). Peaks 1 and 2 (in dashed red) are the result of strong light matter coupling in the $\mathbf{e}_y$ direction, peak 3 is the photonic mode (in dashed blue) resulting from the uncoupled $\mathbf{e}_x$ direction. Note the increasing amplitude of peak 3 and decreasing amplitude of peaks 1 and 2 as $\phi$ is increased. (c) Dispersions of the TE-transmissivity maxima for $\phi$ varying by steps of $1^\circ$: the black

crosses indicate the positions of the maxima for the two peaks in the main signal up until $\phi = 73^{\circ}$, angle from which the two maxima are no longer resolved and replaced by a single maximum, in red the angle-independent positions of the two peaks induced by SC along $\mathbf{e}_y$, in blue the angle-independent position of the photonic mode along $\mathbf{e}_x$. Note that the maxima from the overall signal converge towards the photonic mode energy with increasing $\phi$.

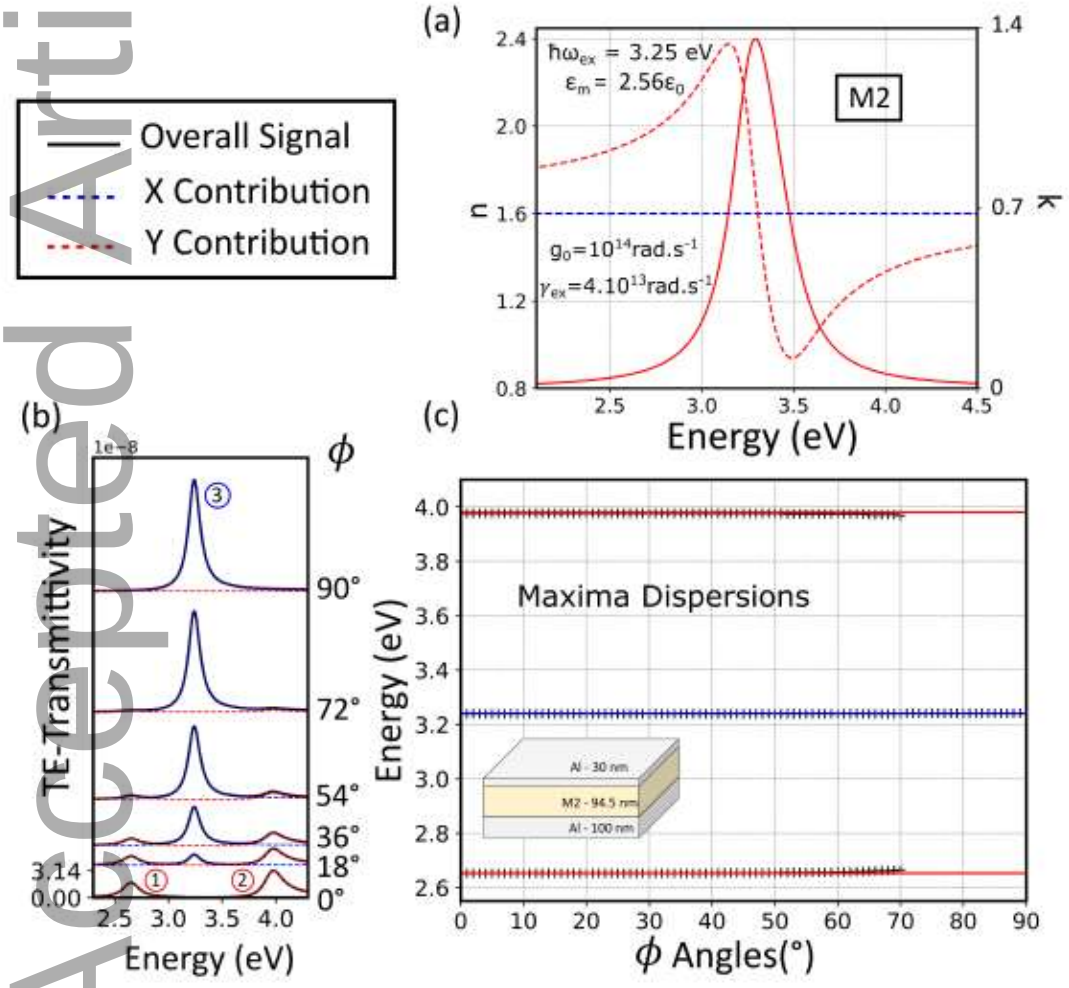


Figure 3: (a) In red and blue respectively ($n_y$, $k_y$) and ($n_x$, $k_x$) optical components for a simulated material M2 with susceptibility $\chi(\omega)$ using the physical parameters in the inset. Dashed lines give the real component of the complex refractive index $\tilde{n} = n + jk$, solid lines the imaginary component. (b) Simulated TE-transmissivity at $\theta = 0^{\circ}$ for $\phi = 0^{\circ}, 18^{\circ}, 36^{\circ}, 54^{\circ}, 72^{\circ}, 90^{\circ}$ of the microcavity

displayed in the inset of (c), the black curves represents the total transmissivity which is a superposition of the transmissivities originating from the $\mathbf{e}_y$ direction (in dashed red) and $\mathbf{e}_x$ direction (in dashed blue). Peaks 1 and 2 (in dashed red) are the result of USC in the $\mathbf{e}_y$ direction, peak 3 is the photonic mode (in dashed blue) resulting from the uncoupled $\mathbf{e}_x$ direction. Note the increasing amplitude of peak 3 and decreasing amplitude of peaks 1 and 2 as $\phi$ is increased. (c) Dispersions of the TE-transmissivity maxima for $\phi$ varying by steps of $1^\circ$: the black crosses indicate the angle-independent positions of the maxima for the well resolved three peaks in the main signal up until $\phi = 70^\circ$, angle from which the two maxima from the $\mathbf{e}_y$ direction are no longer visible, in red the angle-independent positions of the two peaks induced by SC along $\mathbf{e}_y$, in blue the angle-independent position of the photonic mode along $\mathbf{e}_x$. Note that the positions of the maxima in the main signal matches the positions of peak 1, 2 and 3.

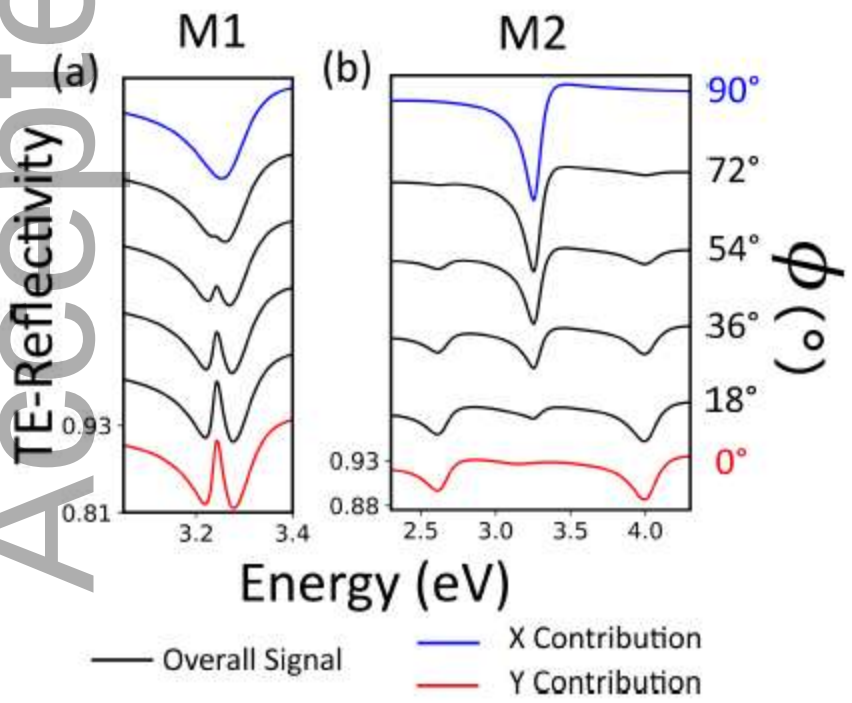


Figure 4: Simulated TE-reflectivity at $\theta = 30^\circ$ for $\phi = 0^\circ, 18^\circ, 36^\circ, 54^\circ, 72^\circ, 90^\circ$ of the microcavities displayed in the inset of Figure 2 (c) for (a) and Figure 3 (c) for (b) with a 99.5 nm material layer

thickness. In both cases the simulated values at $\phi = 0^\circ$ (in solid red) correspond to the reflectivity contributions from the LP and UP in the $\mathbf{e}_y$ direction, the simulated values at $\phi = 90^\circ$ (in solid blue) correspond to the reflectivity contribution from the photonic mode in the $\mathbf{e}_x$ direction. For other values of $\phi$, two main minima are visible in (a) and get closer in energy with increasing values of $\phi$ as the relative reflectivity contribution along $\mathbf{e}_y$ decreases and the one along $\mathbf{e}_x$ increases until only one peak corresponding to the photonic mode $\mathbf{e}_x$ is visible. In (b) three main minima are visible but do not shift in energy with increasing values of $\phi$ as the relative reflectivity contribution along $\mathbf{e}_y$ decreases and the one along $\mathbf{e}_x$ increases.

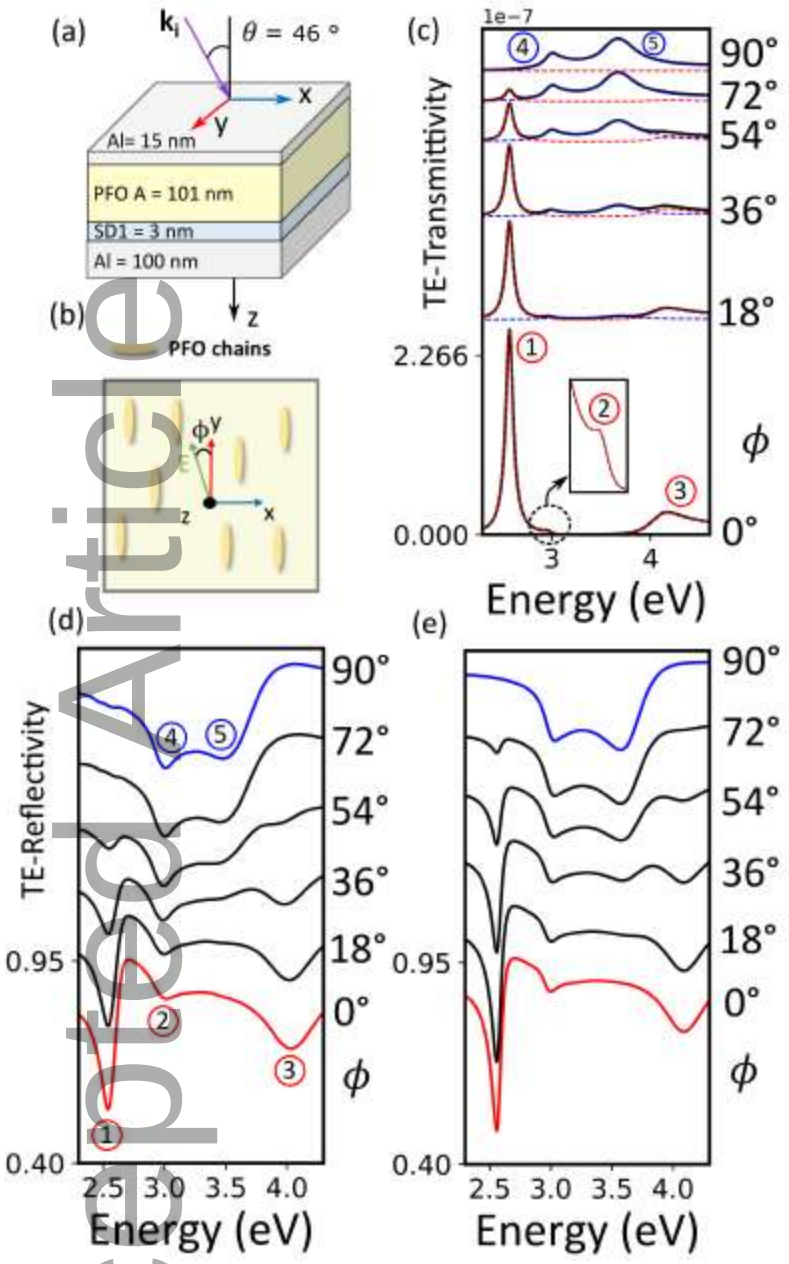


Figure 5: (a) Schematic of the microcavity structure fabricated. The PFO chains were oriented (A) using the protocol presented in Ref 22. The TE-reflectivity is measured at $\theta = 46^{\circ}$. (b) Bottom view of the orientation of the PFO chains along $\mathbf{e}_y$, the measurement is performed by rotating the sample relative to the electric field $\mathrm{E}$ (in green), forming the azimuthal angle $\phi$. (c) Simulated TE-transmissivity at $\theta = 46^{\circ}$ for $\phi = 0^{\circ}, 18^{\circ}, 36^{\circ}, 54^{\circ}, 72^{\circ}, 90^{\circ}$, the black curves represent the total transmissivity which is a superposition of the transmissivities originating from the $\mathbf{e}_y$ direction (in dashed red) and $\mathbf{e}_x$ direction (in dashed blue). Peaks 1, 2 and 3 (in dashed red) are the result of USC

along $\mathbf{e}_y$ for the lowest lying energy cavity mode (1 and 3) and the second lowest lying energy cavity mode (2). Peak 4 and 5 are the result of a splitting of the photonic mode in the $\mathbf{e}_x$ direction due to remaining optical activity. Further explanations can be found in text. (d) Measured TE-reflectivity at $\theta = 46^\circ$ for $\phi = 0^\circ, 18^\circ, 36^\circ, 54^\circ, 72^\circ, 90^\circ$, the numbered minima correspond to the ones simulated in transmissivity. (e) Simulated TE-Reflectivity at $\theta = 46^\circ$ for $\phi = 0^\circ, 18^\circ, 36^\circ, 54^\circ, 72^\circ, 90^\circ$ confirming the experimental observations.